31st Congress of the International Council of the Aeronautical Sciences

Belo Horizonte, Brazil; September 09-14, 2018

THRUST MODELS BASED ON OPERATIONAL FLIGHT DATA USED IN PARAMETER ESTIMATION FOR SAFETY ANALYSES

Phillip Koppitz* , **Jonas Kuerten*** , **Prof. Dr.-Ing. Florian Holzapfel***
***Technical University of Munich, Institute of Flight System Dynamics**

Keywords: *Thrust Model, Operational Flight Data, Parameter Estimation*

Abstract

Based on available operational flight data of a Boeing 737-300 with CFM56-3 engines, four different thrust models are developed in MATLAB. The model development is supported by the software GasTurb which is able to compute operating lines for engine components based on a design point. The results are used for the generation of lookup tables. The computed thrust is then utilized in parameter estimation for the landing phase from touchdown to a calibrated airspeed of 50kts. Here, zero drag coefficients, spoiler drag coefficients and a braking coefficient are estimated for about 1500 flights using the Output Error Method combined with the Gauss-Newton algorithm.

1 Introduction

In order to ensure and increase the safety level of airlines, they are obligated to analyze their operational flight data recorded in so called Quick Access Recorders (QAR). This is an recorder comparable to the flight data recorder, known as *black box* for accident investigation, but containing more parameters and being easily accessible. These data contain valuable safety related information about flight physics, system parameters or aircraft configuration for predictive analysis using physics based incident models, e.g. for the Runway Overrun [1]. The estimation of drag and braking coefficients is essential to be able to simulate landings within a dedicated incident model. For avoiding the estimation of parameters of simple thrust models and to reduce the number of unknown longitudinal forces, the thrust shall be directly determined based on multiple available time series from the QAR and more complex thrust models with fixed parameters to approximate a certain engine type behavior. These models are supported by design calculations in the GasTurb software. This approach differs from existing work by Chati [2] and Campbell [3]. The goal of this paper is to model the longitudinal acceleration during landing using the complex thrust models and by estimating drag and braking coefficients for later usage in physics based incident models at the Institute of Flight System Dynamics.
The results of this paper are based on data of Boeing 737-300 aircraft which are equipped with CFM56-3 engines of variant B2.

2 Thrust Model Development

The overall idea for modeling the thrust is utilizing the software GasTurb [4] to generate lookup tables for the model implementation in MATLAB. GasTurb enables to compute component maps where the relation between relative corrected spool speed, reduced mass flow, isentropic efficiencies and total pressure ratios can be drawn from.

$$T_N = T_{g,II} + T_{g,I} - T_i \tag{1}$$

$$T_i = \dot{m}_0 \cdot V_{TAS} \tag{2}$$

The net thrust T_N of the engine in Eq. (1) is modeled as the sum of the bypass gross thrust $T_{g,II}$, the core gross thrust $T_{g,I}$ and the inlet nozzle momentum T_i with the mass flow $\dot{m}_0$ and the true airspeed V_{TAS}. With the data exports from GasTurb, four different model approaches are tested. The first model is a pure lookup table for the thrust. The other three models share bypass thrust calculation and the same fan compressor map to retrieve corrected engine mass flow, pressure ratios and efficiencies. The core thrust of the second model is determined via a lookup table of the thrust ratio between bypass and core thrust. Models 3 and 4 utilize several component maps within thermodynamic station calculations for the core thrust based on Exhaust Gas Temperature (EGT) and on the fuel flow measurement, respectively. Formulas for the station calculations are based on [5] and [6]. The station designation used in the index of variables is based on the Aerospace Recommended Practice 755C of the Society of Automotive Engineers [7], which is also used in GasTurb [8] and listed here:
0: Ambient; 1: Aircraft engine interface; 2: First compressor/fan inlet; 21: Inner stream fan exit; 13: Outer stream fan exit; 18: Bypass nozzle throat; 25: High pressure compressor (HPC) inlet; 3: HPC exit; 4: Burner exit, high pressure turbine (HPT) inlet; 45: Low pressure turbine (LPT) inlet; 5: LPT exit; 8: Core nozzle throat.

2.1 Modeling in GasTurb

Detailed performance data of is generally not available to the public. This includes the compressor and turbine maps, which are mandatory for engine performance modeling. GasTurb comes with a set of component maps that are scaled in the design process to fit the desired engine.
The simulation in GasTurb consists of two steps, design point modelling and the off-design. For the design point, operating data of a high power setting is suitable [9]. Available engine data usually refers to the maximum power setting of an uninstalled engine on the test bed.[10] Available performance data [11, 12, 13] was used to define the design point, e.g. the Take Off Rating of 98kN. Due to extraction of bleed air or of mechanical power when mounted, the performance of the engine in service is below the maximum uninstalled thrust. The performance reducing quantities need to be estimated. For simplification the extraction of bleed air and mechanical power were assumed to be constant for models 1 and 2. The inlet duct is another contributor to installation losses modelled with the standard GasTurb inlet map.
The off-design results in operating lines of the engine components for the entire operating envelope. An operating line is a set of operating points. Detailed information on the off design and the adjustment of component maps can be found in [8] and [9].

2.2 Model 1: Look-Up Thrust Model

Model 1 is completely based on thrust values calculated by GasTurb. For each operating point GasTurb can provide thrust values which are exported and fed into a lookup table. Several operating lines for different Mach numbers and altitudes were exported to cover the entire flight envelope. Fan speed, Mach number and altitude are the main factors influencing the engine thrust and input parameters to the lookup table. The thrust calculated by GasTurb for different altitudes is based on pressure and temperature according to the International Standard Atmosphere (ISA). The ambient conditions of the QAR-altitude can differ from the ISA conditions and therefore may lead to deviations.

2.3 Using Operating Lines from GasTurb's Component Maps for Thrust Calculation

As the shape of the operating lines primarily changes with respect to the Mach number, the operating lines were exported for different Mach numbers. A set of operating lines of the fan is exemplary given in figure 1. The map data is fed into a 2D look-up table which has the relative corrected component speed and the flight Mach number as inputs. The map based models are independent of ISA conditions since the station cal-

culation is based on the actual ambient pressure and temperature from the QAR data and due to the use of corrected units in the component maps.

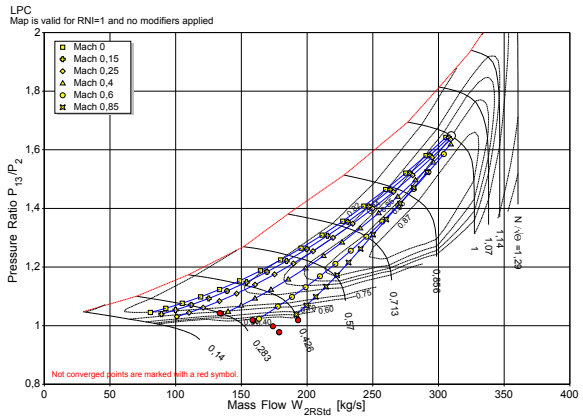

Fig. 1 Fan Map

2.3.1 Bypass Thrust Model based on Fan Map

Models 2,3 and 4 all use the same thrust model for the bypass thrust based on station computations from ambient condition to bypass nozzle throat described in the following.

Total pressure $p_{t,0}$, total temperature $T_{t,0}$ and Mach number are calculated from the static pressure $p_{s,0}$, static temperature $T_{s,0}$ and the true airspeed V_{TAS}.

The engine intake is assumed to be adiabatic, therefore $T_{t,2}$ equals $T_{t,0}$. $p_{t,2}$ is calculated with the inlet pressure recovery, obtained from the inlet map, that is implemented as a 2D look-up table with the Mach number and the relative corrected fan speed as inputs. It is assumed that the pressure loss is the same for core and bypass stream. The corrected engine mass flow, the isentropic efficiency and the pressure ratio of the fan are read from the fan map. With the fan intake conditions $T_{t,2}$ and $p_{t,2}$ the corrected engine mass flow can be converted to the actual mass flow $\dot{m}_0$. The bypass ratio (BPR) varies depending on spool speed and Mach number. The BPR is exported similar to the operating lines from GasTurb and fed into a lookup table. With the BPR the core mass flow $\dot{m}_I$ and the bypass mass flow $\dot{m}_{II}$ are calculated from the engine mass flow $\dot{m}_0$.

$$p_{t,13} = p_{t,2} \cdot \Pi_{t,fan} \tag{3}$$

$$T_{t,13} = T_{t,2} \cdot \left(1 + \frac{\Pi_{t,fan}^{\frac{\bar{\gamma}-1}{\bar{\gamma}}} - 1}{\eta_{is,fan}} \right) \tag{4}$$

The fan map can be split into an inner and outer part. For the bypass thrust the outer part is of interest. The total pressure $p_{t,13}$ and total temperature $T_{t,13}$ at the fan exit are given in Eqs. (3) and (4), where $\Pi_{t,fan}$ is the outer pressure ratio of the fan and $\eta_{is,fan}$ its isentropic efficiency.

The specific heat capacity $\bar{c}_p$ and the specific heat ratio $\bar{\gamma}$ are calculated with the mid-temperature and the fuel to air ratio (FAR) of the gas which is covered by a polynomial given in [5] and based on the work of S. Gordon and B. J. McBride [14]. The mid-temperature of each compression or expansions is found in an iterative process of calculating the exit temperature of the considered component. For the compression in fan, booster and HPC the FAR is zero. The bypass duct is assumed to be adiabatic, therefore $T_{t,18}$ equals $T_{t,13}$. The pressure loss within the bypass duct and the bypass nozzle is assumed to be constant. The convergent nozzle has two operating conditions, which are determined by the critical pressure ratio at the throat of the nozzle:

$$\left(\frac{p_{t,18}}{p_{s,0}} \right) \gtrless \left(\frac{p_t}{p_s} \right)_{crit} = \left(1 + \frac{\gamma_{18} - 1}{2} \right)^{\frac{\gamma_{18}}{\gamma_{18}-1}} \tag{5}$$

If the pressure ratio at the nozzle throat is larger than the critical pressure ratio, the nozzle is choking ($Ma_{18} = 1$). In the choked condition the static pressure is above the ambient pressure. With Mach number $Ma_{18} = 1$ the static temperature $T_{s,18}$ and pressure $p_{s,18}$ can be calculated from the total temperature $T_{t,18}$ and pressure $p_{t,18}$. The exit velocity c_{18} equals the local speed of sound in Eq. (6) with gas constant R_0.

$$c_{18} = \sqrt{\gamma_{18} \cdot R_0 \cdot T_{s,18}} \tag{6}$$

For the unchoked nozzle the ambient pressure $p_{s,0}$ equals the static pressure $p_{s,18}$ at the throat of

the nozzle. The exit velocity c_{18} can be derived from difference of the total and static specific enthalpy $(h_{t,18} - h_{s,18})$ and the isentropic relation, Eq. (7).

$$c_{18} = \sqrt{2 \cdot c_{p_{18}} \cdot T_{t,18} \cdot \left(1 - \left(\frac{p_{s,18}}{p_{t,18}}\right)^{\frac{\gamma_{18}-1}{\gamma_{18}}}\right)} \tag{7}$$

All parameters for calculating the bypass gross thrust $T_{g,II}$ in Eq. (8) are known at this stage. In case of the unchoked nozzle, the additional thrust resulting from the pressure difference $p_{s,18} - p_{s,0}$ at the exit area A_{18} is zero.

$$T_{g,II} = \dot{m}_{II} \cdot c_{18} + A_{18} \cdot (p_{s,18} - p_{s,0}) \tag{8}$$

2.3.2 *Model 2: Core Thrust based on Thrust Ratio*

The core gross thrust for model 2 $T_{g,I,2}$ for Eq. (1) is obtained from the ratio of the core and bypass gross thrust Φ, which is exported from GasTurb similar to the operating lines. GasTurb allows the user to compose parameters out of available standard parameters. The data is fed into a 2D lookup table with the relative corrected fan speed and the Mach number as input parameters.

2.3.3 *Model 3: Core Thrust based on EGT-Signal*

The core thrust of model 3 is based on the EGT-signal of the QAR-data. The total temperatures and total pressures at stations 21, 25 and 3 of the core engine are calculated with the operating lines of the inner fan, the booster and the HPC similar to Eqs. (3) and (4). The bleed air $(\dot{m}_b)$ is assumed to be extracted behind the HPC. The reduction of the core mass flow and the HPC pressure ratio by extraction of bleed air is taken into account. The model also considers the drain of mechanical power (P_{ext}) that is extracted from the N2 spool. In the combustion chamber the fuel mass flow $\dot{m}_f$ is added. The total pressure loss in the combustion chamber is set to 5 %. With the core mass flow $\dot{m}_I$, the dynamic pressure $p_{t,4}$ and the EGT-data, the exit conditions of the HPT and LPT can be calculated with the power balance of the N1 and N2 spool.

The EGT is measured in the stator of the second LPT-stage. The EGT-measurement in the CFM56-3 is described in Kurzke [15] in detail. Since the LPT has four stages with increasing blade diameter, the work extraction is not constant across the four stages. The temperature decrease after the first stage can be estimated to $\beta_{EGT} = 0.217$ as described in [15]. As the thermocouple measuring the EGT is located within a stator and is not aligned with the direction of the gas flow, a recovery factor $\alpha_{EGT} = 0.976$ for the EGT measurement is introduced. [15] For the calculations α_{EGT} and β_{EGT} were assumed to be constant throughout the operating envelope.

$$\frac{EGT}{\alpha_{EGT}} = T_{t,45} - \beta_{EGT} \cdot \left(T_{t,45} - T_{t,5}\right) \tag{9}$$

The power of fan P_{fan} and booster $P_{booster}$ are calculated with the mass flow, temperature difference and $\bar{c}_p$ of each component. With the assumption of a constant mechanical efficiency of the N1 spool η_{N1} the power of the LPT P_{LPT} is:

$$P_{LPT} = \frac{P_{fan} + P_{booster}}{\eta_{N1}} \tag{10}$$

$$P_{LPT} = \left(\dot{m}_I + \dot{m}_f - \dot{m}_b\right) \cdot \bar{c}_p \cdot \left(T_{t,45} - T_{t,5}\right) \tag{11}$$

The temperature difference in Eq. (9) is a factor in the calculation of the LPT power P_{LPT} in Eq. (11). Combining Eqs. (9) and (11) leads to an expression for $T_{t,45}$ in Eq. (12) where $\bar{c}_p$ and $T_{t,45}$ can again be calculated iteratively using the before mentioned polynomial. With $\bar{c}_p$ and $T_{t,45}$, the total temperature $T_{t,5}$ can be calculated with Eq. (11).

$$T_{t,45} = \frac{EGT}{\alpha_{EGT}} + \beta_{EGT} \cdot \left(\frac{P_{LPT}}{\bar{c}_p \cdot \left(\dot{m}_I - \dot{m}_b + \dot{m}_f\right)}\right) \tag{12}$$

$$p_{t,45} = p_{t,4} \cdot \left(1 - \frac{1}{\eta_{is,HPT}}\left(1 - \frac{T_{t,45}}{T_{t,4}}\right)\right)^{\frac{\bar{\gamma}}{\bar{\gamma}-1}} \tag{13}$$

The total pressure at station 45 $p_{t,45}$ is obtained from Eq. (13), which can be derived from the

isentropic relation and the definition of the isentropic efficiency. The isentropic efficiency of the HPT ($\eta_{is,HPT}$) is stored in a 2D look-up table with the Mach number and the relative corrected HPT spool speed as inputs. The total temperature $T_{t,4}$ is obtained from the power balance of the N2-spool. The total pressure at station 5 is calculated in the same way by inserting $T_{t,45}$, $T_{t,5}$, $p_{t,45}$ and $\eta_{is,LPT}$ into Eq. (13).
The core nozzle condition and exit velocities are computed similarly to the bypass nozzle. The resulting gross thrust of the core for Eq. (1) is given in Eq. (14), where in case of an unchoked core nozzle the thrust resulting from the pressure difference is again zero.

$$T_{g,I,3} = \left(\dot{m}_I - \dot{m}_b + \dot{m}_f\right) \cdot c_8 + A_8 \cdot (p_{s,8} - p_{s,0}) \tag{14}$$

2.3.4 *Model 4: Core Thrust based on Fuel Flow Rate*

Models 3 and 4 share the same calculations of the core till station 3. With a simplified combustion calculation, which is based on the equations in W. Bräunling [5], the burner exit temperature $T_{t,4}$ can be calculated with use of the fuel flow rate. The energy balance between the stations 3 and 4 is given in Eq. (15), where LCV is the lower calorific value of the kerosene at a reference temperature of $T_{ref,k}$ =298,15 K and η_c the combustion efficiency.[5]

$$\begin{aligned}&\left(\dot{m}_I - \dot{m}_b + \dot{m}_f\right) \cdot h_{t,3} = \\ &\left(\dot{m}_I - \dot{m}_b\right) \cdot h_{t,4} + \dot{m}_f \cdot \eta_c \cdot LCV\end{aligned} \tag{15}$$

With the enthalpy $h_{t,4}$ [5]:

$$h_{t,4} = \bar{c}_p\Big|_{T_{ref,k}}^{T_{t,4}} \cdot \left(T_{t,4} - T_{ref,k}\right) \tag{16}$$

With Eq. (16) and Eq. (15), $T_{t,4}$ is obtained iteratively. The specific heat capacity c_p is averaged over the evaluations at $T_{ref,k}$ and $T_{t,4}$. [5]. The temperatures at stations 45 and 5 again can be obtained from the power balance of the N1 and N2 spools. The pressures $p_{t,45}$, $p_{t,5}$, exit velocity c_8, core gross thrust $T_{g,I}$ and engine net thrust T_N are calculated similarly to model three.

2.4 Sensitivity of Fixed Model Parameters

Since not all fixed model parameters were known, especially for the models 3 and 4, they had to be assumed. Therefore, the sensitivity of the thrust with respect to certain model parameters was analyzed. Model parameters taken into account were total pressure losses in the bypass duct, the core engine nozzle and the combustion chamber. Further parameters are the amount of bleed air, the power drain, mechanical efficiencies and the combustion efficiency. The most influencing parameters are the EGT-correction factor α_{EGT}, the bleed air mass flow $\dot{m}_b$ and the combustion efficiency η_c.

3 Thrust Model Comparison

Within the following subsections the computed thrust from the four described models will be shown as well as analyses of the differences between the models for multiple flights.

3.1 Single Flight Analysis

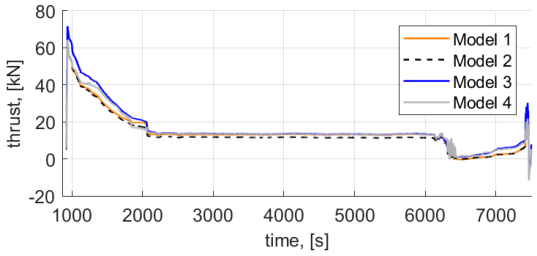

Fig. 2 Thrust for complete flight, single engine

The described models lead to similar thrust values resembling the expected behavior during one flight as depicted in Fig. 2. During take off the thrust of a single engine increases to a maximum value at 25m/s ground speed between 64kN for models 1,2 and 4 to 72kN for model 3. This is between 65.3% and 73.5% of the Take Off Rating under standard conditions and without taking into account power losses when mounted. Decreasing thrust during the climb phase and a drop in thrust at level off fit the expected behavior as well. During descend and approach the thrust de-

creases again before it increases during final approach when flaps and landing gear are extended. Within Fig. 3 it is zoomed in to the landing phase. In addition to the pure thrust computation also the effect of deployed reversers can be seen.

$$T_{N,rev} = T_{g,I} + c_{rev} \cdot T_{g,II} - T_i \tag{17}$$

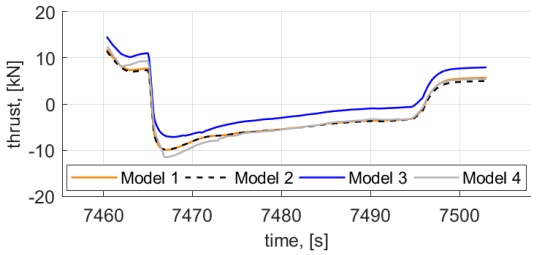

Fig. 3 Thrust during landing phase, single engine

The CFM56-3 uses a cold stream reverser that deflects the bypass stream by a certain angle δ_{rev}. This is taken into account with the factor c_{rev} in the net thrust during deployed reversers $T_{N,rev}$ in Eq. (17), which is similar to Eq. (1). For a smooth transition, over-critically damped PT2 behavior is assumed for c_{rev} when changing from $c_{rev} = 1$ to $c_{rev} = \sin\delta_{rev}$.
The graphs in Fig. 3 show flight idle thrust at touchdown and the deployment of the reversers about 5 seconds later. Once the reversers are deployed, no run up of the fan speed for additional reversed thrust is commanded by the pilot. Therefore the reversed thrust decreases during deceleration phase and changes back to positive thrust once the reversers are stowed.
The differences between the models 2, 3 and 4 four steam from the core thrust computation only. Since the parameter estimation is applied to the landing phase, a closer look is taken on the thrust difference for this phase in the next section.

3.2 Model Differences for Multiple Flights

In order to compare the models' performance for multiple flights, metrics need to be defined. For this analysis it was chosen to look at the error time series $\Delta T(k)$ between the net thrust of the first model $T_{N,1}$ and of each one of the other models $T_{N,x}$ as defined in Eq. (18). The actual metrics for this case are the mean value $\mu(\Delta T)$ of these errors and the standard deviation $\sigma(\Delta T)$, given in Eq. (19) and (20). It is sufficient to look at the resulting three pairs since all other pairs can be computed from them.

$$\Delta T(k) = T_{N,1}(k) - T_{N,x}(k) \tag{18}$$

$$\mu(\Delta T) = \frac{1}{n}\sum_{k=1}^{n} e_T(k) \tag{19}$$

$$\sigma(\Delta T) = \sqrt{\frac{1}{n-1}\sum_{k=1}^{n}\left[e_T(k) - \mu(\Delta T)\right]} \tag{20}$$

Additionally it is distinguished between time steps k when the reversers are deployed and when they are stowed. In the following figures only the results for deployed reversers are shown, where on the left side mean values and on the right side standard deviations can be seen.

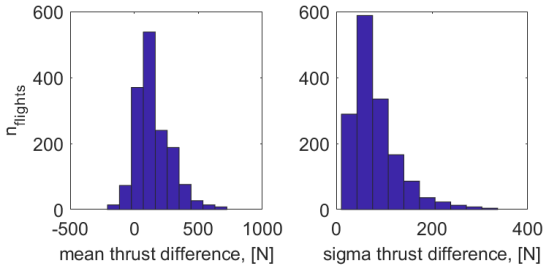

Fig. 4 Thrust difference between Models 1 and 2

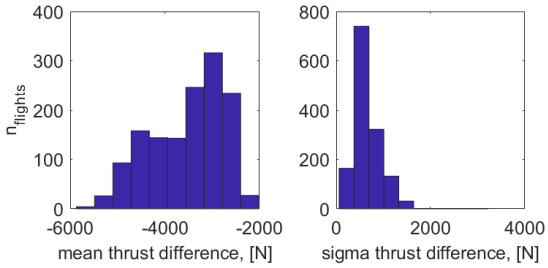

Fig. 5 Thrust difference between Models 1 and 3

The differences between models 1 and 2 in Fig. 4 show the most stable behavior over all flights. This can be explained by model 2 still using a look up table for the core thrust together

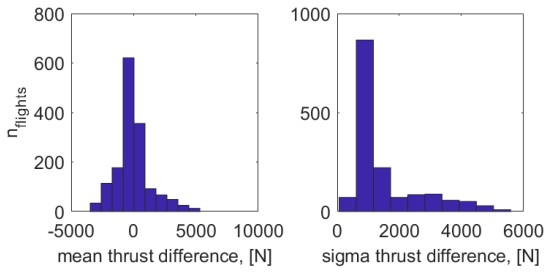

Fig. 6 Thrust difference between Models 1 and 4

with the more simple computation of the fan thrust. The extreme differences at the edges of the distribution can be explained by significantly different environmental conditions compared to the standard atmosphere assumed in model 1. A clear offset towards higher thrust values in model 3 compared to model 1 together with higher standard deviations can be seen in Fig. 5. This might be caused by wrong measurements of EGT and model assumptions for the core thrust computation. The mean values of the differences between model 1 and 4 (Fig. 6) show the highest spread of values and even higher standard deviations for each single flight. This leads to the conclusion that the fuel flow data as well as the modelling approach contain high uncertainty.

4 Parameter Estimation during Landing

With the thrust models developed the estimation of drag and friction coefficients is possible. Since recording operational flight data is not done for the purpose of parameter estimation as it is done for flight test campaigns, the data have poor recording frequency and little excitation of system dynamics. Therefore, the number of observable parameters is generally very limited.
As a first method we decided for the Output Error Method (OEM) which is rather simple but still provides more flexibility than least squares algorithms, e.g possibility to bound parameters.

4.1 Output Error Method

This section describes the implementation of the iterative Output Error Method based on [16]. For this paper where one output $z(t)$ is used for the estimation.

$$y_i(t) = g(\boldsymbol{u}(t), \boldsymbol{\Theta}_i) \tag{21}$$

$$r_i(t) = z(t) - y_i(t) \tag{22}$$

$$J(\boldsymbol{\Theta}_i) = \sigma^2(r_i(t)) \tag{23}$$

The time variant output $y_i(t)$ for iteration i is calculated by the algebraic output function g with input time series $\boldsymbol{u}(t)$ and the model parameters $\boldsymbol{\Theta}_i$, Eq. (21). With the residual $r_i(t)$ in Eq. (22) the cost function J is defined as its variance in Eq. (23). Time variant variables are implemented as row vectors. For calculating the parameter update $\Delta\boldsymbol{\Theta}_i$ within each iteration, the Gauss-Newton algorithm is implemented as follows:

$$\Delta\boldsymbol{\Theta}_i = -\left(\frac{\partial^2 J(\boldsymbol{\Theta}_i)}{\partial \boldsymbol{\Theta}^2}\right)^{-1} \frac{\partial J(\boldsymbol{\Theta}_i)}{\partial \boldsymbol{\Theta}} \tag{24}$$

, with the second derivative of the cost function

$$\frac{\partial^2 J(\boldsymbol{\Theta}_i)}{\partial \boldsymbol{\Theta}^2} = \left(\frac{\partial y_i(t)}{\partial \boldsymbol{\Theta}}\right)^T \cdot \sigma^2(r_i(t)) \cdot \frac{\partial y_i(t)}{\partial \boldsymbol{\Theta}}, \tag{25}$$

and the first derivative of the cost unction

$$\frac{\partial J(\boldsymbol{\Theta}_i)}{\partial \boldsymbol{\Theta}} = -\left(\frac{\partial y_i(t)}{\partial \boldsymbol{\Theta}}\right)^T \cdot \sigma^2(r_i(t)) \cdot r_i(t). \tag{26}$$

The sensitivity $\frac{\partial y_i(t)}{\partial \boldsymbol{\Theta}}$ is determined symbolically and is hard coded for higher accuracy and computational speed. If the relative change in the cost function between iterations is small enough, the current parameters are used as result. If the cost function increases, the current step $\Delta\boldsymbol{\Theta}_i$ is halved within one iteration.

4.2 Model Equations for Parameter Estimation

The longitudinal acceleration a_x as output $y(t)$ is influenced by four different forces, the net thrust T_N, the drag D, the braking force F_B and the gravitational force F_G due to runway slopes.

$$a_x = (T_N + D + F_B + F_G)/m \tag{27}$$

Because of the data quality, simplified models for the drag force D in Eq. (28) and braking force F_B in Eq. (29) were chosen.

$$D = \bar{q} \cdot S \cdot (C_{D0} + C_{D,sp} \cdot \delta_{sp}) \tag{28}$$

with the estimated coefficients for zero drag C_{D0}, drag due to spoiler deflection $C_{D,sp}$, the dynamic pressure $\bar{q}$, the wing reference are S, and the spoiler deflection δ_{sp}. A hypothesis is, that the aerodynamic coefficients show close to constant behavior if the model represents main effects.

$$F_B = C_B \cdot \frac{p_{br}}{p_{br,max}} \cdot F_N \tag{29}$$

The braking force F_B in Eq. 29 is computed with the estimated friction coefficient C_B, the brake pressure p_{br}, the maximum brake pressure $p_{br,max}$, and the normal force at the landing gear F_N. The normal force includes a simple model for the lift with assumed coefficients. In contrast to the aerodynamic coefficients, the friction coefficient should vary with different environmental conditions. The model includes three parameters $\boldsymbol{\Theta} = [C_{D0}, C_{D,sp}, C_B]$ to be estimated and its main inputs $\boldsymbol{u}(t)$ include the thrust model inputs, dynamic pressure $\bar{q}$, spoiler deflection δ_{sp}, and the brake pressure p_{br}.

4.3 Single Flight Analysis

The initial step was to analyze a limited number of single flights by plotting a proof of match as well as the residuals for all four thrust models, see Fig 7.

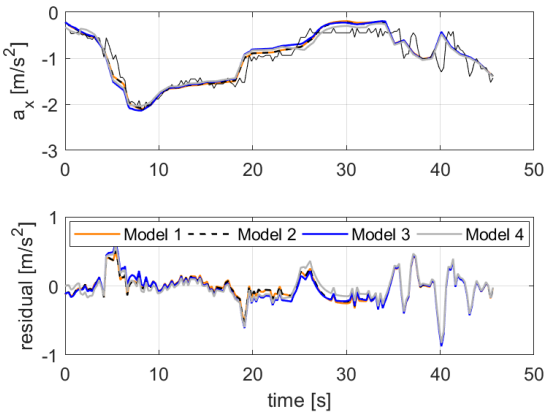

Fig. 7 Proof of match for single flight

Table 1 Estimated parameters for single flight

Model	1	2	3	4
C_{D0}	0.1494	0.1466	0.1645	0.1389
$\sigma(C_{D0})$	0.0054	0.0053	0.0059	0.0056
$C_{D,sp}$	0.1545	0.1588	0.1959	0.2022
$\sigma(C_{D,sp})$	0.011	0.011	0.012	0.011
C_B	0.9160	0.8895	0.9557	0.9041
$\sigma(C_B)$	0.025	0.025	0.028	0.026

All modelled longitudinal accelerations follow the main trends of the measured one. The retraction of the reversers at 20s as well as braking action at the end of the time series are captured. The residuals are very similar but show deterministic behavior at the beginning when spoilers are deployed and at the end during braking. This is confirmed by tests for whiteness and normality for the residual and most probably caused by time shifts.

The estimated parameters and their standard deviations σ in Tab. 1 do not differ significantly between the used thrust models. Results for Model 3 show greater deviations from the rest. The correlations between the parameters based on the input data and the Fisher Matrix show high correlations between C_{D0} and $C_{D,sp}$, but little correlation of both with the friction coefficient C_B. However, based on the proof of match for a single flight, given the low quality of the data and model uncertainties, the parameters don't necessarily fulfill the hypothesis mentioned in the previous section.

4.4 Statistics over Available Flights

After showing the parameter estimation for a single flight, the estimation is now executed for all available flights using the second thrust model. After excluding results where $\sigma(C_{D,sp}) > 0.2$ and $\sigma(C_B) > 0.5$, parameters for 1384 flights are available.

The results show a spread for both drag coefficients in Fig. 8 and 9. The simple model, strong correlation, interference with the braking action, data errors as well as time shifts between longitudinal acceleration and spoiler deflection can

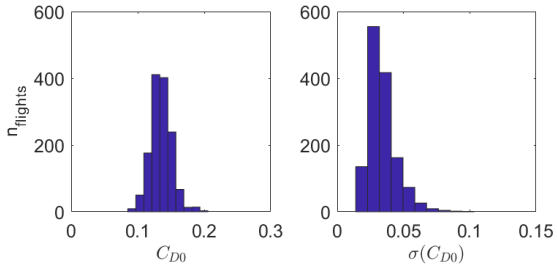

Fig. 8 Estimated zero drag coefficient

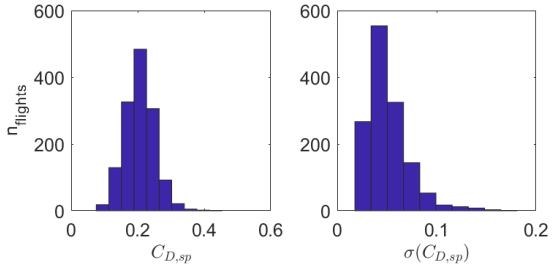

Fig. 9 Estimated spoiler drag coefficient

be explanations. The brake coefficient C_B in Fig. 10 shows non-physical negative values as well as outliers above 1.5. The negative values are due to simultaneous start of braking and spoiler deployment for some flights or minor braking right at the end of the analyzed time series. Some flights with positive outliers have a data error in the spoiler deflection leading to disturbed normal forces. With the currently estimated brake coefficient no clear correlation to precipitation indicated in METAR weather information could be detected. The precipitation is the only, but of course not perfect indication of runway conditions available.

When looking at the distributions of the parameters themselves, see Tab. 2, the standard deviations of the aerodynamic coefficients over all flights are recognized as smaller than most stan-

Table 2 Distribution details of estimated parameters

parameter	mean	standard deviation
C_{D0}	0.135	0.016
$C_{D,sp}$	0.207	0.044
C_B	0.900	0.214

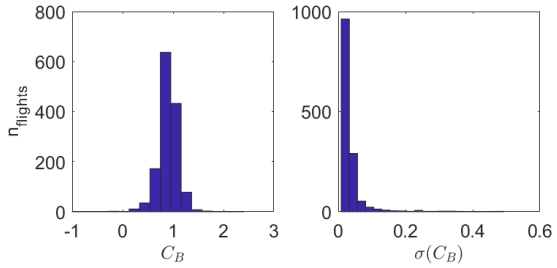

Fig. 10 Estimated brake coefficient

dard deviations $\sigma(C_{D0})$ and $\sigma(C_{D,sp})$ for the single flights. The braking coefficient shows opposite behavior for merely all flights. This corresponds to the hypothesis for the coefficients stated in section 4.2.

With these initial results, a second estimation is done with fixed values for $C_{D0} = 0.135$ and $C_{D,sp} = 0.2$ and only the brake coefficient C_B being estimated. This reduces the number of negative values, but it does not increase the correlation with runway conditions.

Filtering the results for flights with an early start of braking $t_{br} < 2$ and flights with late braking action $t_{br} > 30s$ leads to significant differences in the mean value of the brake coefficient C_B. From this the dependence of the braking effect on the current velocity can be shown.

5 Conclusion and Outlook

The developed thrust models are applicable to all flight phases. Challenges are gathering the necessary engine data and choosing model parameters based on engineering judgment. Publicly available data relates to measurements in a test environment and not the real application. The current status of the thrust models allow parameter estimation during landing and applications in other flight phases will be tested. This first approach to estimating safety critical parameters for incident analyses based on computed thrust opens the way for further work. The results for single flights show good matches between modelled and measured outputs. However, application to a large number of fights shows the need for treatment of data issues as well as modelling different effects in different flights. Future work will in-

clude extensive analyses of statistical dependencies between estimated parameters and influencing factors, bounding of parameters during estimation, development of quality measures as well as model revisions.

References

[1] International Air Transportation Conference. *Safety Report 2013*. Montreal, Geneva, 2014.

[2] Chati Y S and Balakrishnan H. Aircraft Engine Performance Study Using Flight Data Recorder Archives. *AIAA Aviation Technology, Integration, and Operations Conference*, Reston, Virginia, 2013.

[3] Campbell A and Cheng A. Uncertainty Analysis for Calculating Reverse Thrust using In Situ Data. *16th AIAA Aviation Technology, Integration, and Operations Conference*, Washington, DC, 2016.

[4] GasTurb GmbH. accessed 2018 Feb 02. URL: http://www.gasturb.de/index.html

[5] Bräunling W J G. *Flugzeugtriebwerke: Grundlagen, Aero-Thermodynamik, ideale und reale Kreisprozesse, thermische Turbomaschinen, Komponenten, Emissionen und Systeme*. 4th edition, VDI Buch, 2015.

[6] Rick H. *Gasturbinen und Flugantriebe: Grundlagen, Betriebsverhalten und Simulation*. VDI Buch, 2013.

[7] Society of Automotive Engineers SAE. *Aircraft Propulsion System Performance Station Designation and Nomenclature, Aerospace Recommended Practice 755C*. Warrandale, USA, 2013.

[8] GasTurb GmbH. *GasTurb13 - Manual: Design and Off-Design Performance of Gas Turbines*. 2017.

[9] Kurzke J. How to Create a Performance Model of a Gas Turbine From a Limited Amount of Information. *ASME Turbo Expo*. New York, USA, pp 145-153, 2005.

[10] Walsh P P and Fletcher P. *Gas Turbine Performance*. Blackwell Science Ltd, 2004.

[11] European Aviation Safety Agency. *Type-Certificate Data Sheet: E.066 CFM International S.A. - CFM56-2/-3 series engines*. 2008.

[12] Epstein N. CFM56-3 high by-pass technology for single aisle twins. *AIAA International Air Transportation Conference*. Atlantic City, NY, 1981.

[13] Rodrigues Martins D A. Off-Design Performance Prediction of the CFM56-3 Aircraft Engine *Instituto Superior Técnico*. Master Thesis, Lissabon, 2015.

[14] Mc Bride B J et al. *Thermodynamic Properties to 6000 K for 210 Substances Involving the 18 First Elements*. NASA Lewis Research Center, Cleveland, OH, 1963.

[15] Kurzke J. A Physics Based Methodology for Building Accurate Gas Turbine Performance Models *22nd ISBAE Conference*. Phoenix, AZ, 2015.

[16] Jategaonkar R V. *Flight Vehicle System Identification: A Time Domain Methodology*. AIAA, 2006.

Contact Author

Phillip Koppitz
Technical University of Munich
Institute for Flight System Dynamics
Boltzmannstr. 15
85748 Garching, Germany

Email: phillip.koppitz@tum.de
Phone: +49 89 289 16569

Copyright Statement